Ocean Sci., 11, 1–15, 2015
www.ocean-sci.net/11/1/2015/
doi:10.5194/os-11-1-2015

Ocean Science Open Access EGU

Evaluating the surface circulation in the Ebro delta (northeastern Spain) with quality-controlled high-frequency radar measurements

P. Lorente[1], **S. Piedracoba**[2], **J. Soto-Navarro**[1], **and E. Alvarez-Fanjul**[1]

[1]Puertos del Estado, Avenida del Partenón 10, 28042, Madrid, Spain
[2]University of Vigo, Marcosende s/n, 36310, Vigo, Pontevedra, Spain

Correspondence to: P. Lorente (plorente@puertos.es)

Received: 16 July 2015 – Published in Ocean Sci. Discuss.: 24 August 2015
Revised: 28 October 2015 – Accepted: 12 November 2015 – Published:

Abstract. The Ebro River delta is a relevant marine protected area in the western Mediterranean. In order to promote the conservation of its ecosystem and support operational decision making in this sensitive area, a three-site standard-range (13.5 MHz) CODAR SeaSonde high-frequency (HF) radar was deployed in December 2013. The main goal of this work is to explore basic features of the sea surface circulation in the Ebro deltaic region as derived from reliable HF radar surface current measurements. For this aim, a combined quality control methodology was applied: firstly, 1-year long (2014) real-time web monitoring of nonvelocity-based diagnostic parameters was conducted to infer both radar site status and HF radar system performance. The signal-to-noise ratio at the monopole exhibited a consistent monthly evolution, although some abrupt decreases (below 10 dB), occasionally detected in June for one of the radar sites, impacted negatively on the spatiotemporal coverage of total current vectors. It seemed to be sporadic episodes since radar site overall performance was found to be robust during 2014. Secondly, a validation of HF radar data with independent in situ observations from a moored current meter was attempted for May–October 2014. The accuracy assessment of radial and total vectors revealed a consistently high agreement. The directional accuracy of the HF radar was rated at better than 8°. The correlation coefficient and root mean square error (RMSE) values emerged in the ranges [0.58–0.83] and [4.02–18.31] cm s^{-1}, respectively. The analysis of the monthly averaged current maps for 2014 showed that the HF radar properly represented basic oceanographic features previously reported, namely, the predominant southwestward flow, the coastal clockwise eddy confined south of the Ebro delta mouth, or the Ebro River impulsive-type freshwater discharge. The EOF analysis related the flow response to local wind forcing and confirmed that the surface current field evolved in space and time according to three significantly dominant modes of variability.

1 Introduction

The circulation in the Ebro continental margin (northeastern Spain, Fig. 1a) is mainly thermohaline and characterized by a quasi-permanent barotropic shelf-slope jet, which flows southwestwards and is named the North Current, only altered by clockwise inertial oscillations and some short periods of current reversals. This relatively low-intensity current flow (10 cm s^{-1}) is in geostrophic balance with the so-called Catalan front, which is a permanent density front associated with strong salinity gradients maintained by the Ebro River runoff (Font et al., 1988a).

The marine circulation near the delta, although dominated by the alongshore large-scale dynamics, presents a complex structure strongly influenced by the topography, the seasonality of the remarkable Ebro River discharges (Font et al., 1988b), the changing wind conditions and the water column thermal stratification (Salat et al., 2002). Nonetheless, the tidal influence in the continental shelf currents field is very weak, as expected for a microtidal and low-energy environment (Jimenez et al., 2002).

Since the Ebro River delta is one of the most relevant marine protected areas in the western Mediterranean in terms of biodiversity, an intense monitoring activity is performed to manage this deltaic coastal region and promote the conservation of its ecosystem. In order to support marine do-

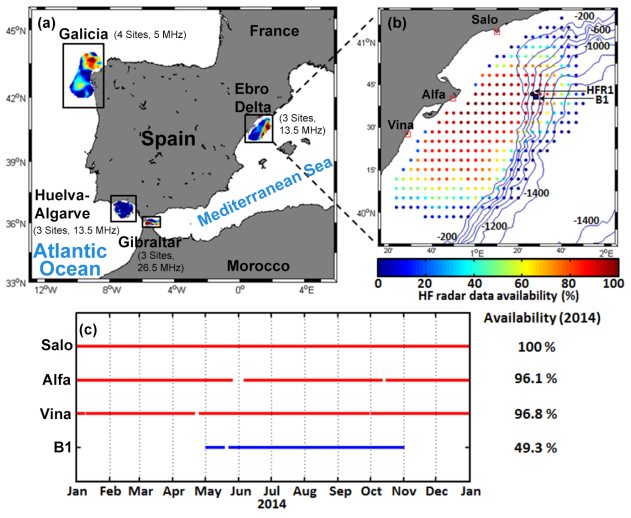

Figure 1. (a) HF coastal radar network currently operated by Puertos del Estado; **(b)** HF radar deployed at the Ebro delta, composed of three sites: Salou (SALO), Alfacada (ALFA) and Vinaroz (VINA). Colored dots denote the temporal coverage in percent of HF radar surface current total vectors for the entire year of 2014. Isobath depths are labeled every 200 m. The location of the Tarragona buoy (B1) is marked with filled blue squares. HFR1 denotes the radar grid point closest to the B1 position. **(c)** Timelines of HF radar sites (red) and B1 buoy (blue) current data availability for 2014.

main awareness and operational decision making in this sensitive area, a network of 13.5 MHz CODAR SeaSonde high-frequency (HF) radar systems has been deployed (Fig. 1b). HF radar has been steadily gaining recognition as an efficient land-based remote sensing instrument for mapping surface currents at high spatial and temporal resolutions in near real time. This technology presents a broad range of practical applications, encompassing management (SAR operations, oil spill emergencies), commercial (vessel tracking, ocean energy production) and research (ecology, water quality, fisheries) uses. Other emerging uses include the validation of operational ocean forecasting systems or assimilation into numerical coastal circulation models (Marmain et al., 2014; Stanev et al., 2015).

As a consequence, there is a growing demand for quality-controlled HF radar surface current measurements. Since HF radar estimations are subject to many potential uncertainties (namely, power-line disturbances, radio frequency interferences, ionosphere clutter, ship echoes, antenna pattern distortions or environmental noise – see Kohut and Glenn, 2003), many efforts have been recently devoted to identifying occasional non-realistic radar current vectors. Such artifacts (defined as spikes, spurious values or corrupted data) are generally detected at the outer edges of the radar domain and flagged in accordance with a pre-defined protocol. An individual quality control (QC) index, based on an integer number derived from a battery of tests, should be assigned for each and every single radar grid cell to indicate the quality level of each measured value (Gomez et al., 2015).

The artifacts can be subsequently eliminated from the data stream in real time (Cosoli et al., 2012b) or offline (Liu et al., 2014). Other approaches are focused, in addition, on replacing noisy values with more reliable estimates (Wyatt et al., 2015) by using open-boundary model analysis (Kaplan and Lekien, 2007) or statistical mapping (Barrick et al., 2012). However, the main drawback lies with the potential removal of accurate data when the discriminating algorithm is based on tight thresholds. Some fine-tuning, based on the specific local conditions of the system, is thus required to have the right tradeoff between confirmed outlier identification and false alarm rate, maximizing the benefit of the applications of these methods (Gomez et al., 2014).

Whereas some quality indexes are assigned according to velocity-based QC schemes, other approaches intend to use nonvelocity-based metrics related to the characteristics of the received signal in order to implement advanced quality controls and reduce the systematic errors in radar current estimates (Kirincich et al., 2012). One of the radial metrics that offers the most potential benefits as a reliability indicator is the signal-to-noise ratio of sea echo at the monopole (SNR3), since it has been previously proven to be a valid proxy for both radar site status and onset of HF radar system malfunction (Cosoli et al., 2012b; Roarty et al., 2012). Complementarily, a big jump in the average state over time in antenna parameters (e.g., amplitude corrections for loops 1 and 2 to the monopole, AMP1 and AMP2, respectively) may indicate an antenna problem and should be investigated (COS, 2005).

In this context, a number of previous works have focused on defining optimum threshold levels since there is still no worldwide consensus. Atwater and Heron (2011) showed that a simple thresholding of SNR3 is a good starting point, although a 20 dB limit constitutes too severe a QC criterion, with a resulting detrimental impact on coverage area. Values of SNR3 below 10 dB have been proved to be closely linked to a significant decrease in the Multiple Signal Characterization (MUSIC) direction-finding algorithm skill (De Paolo and Terril, 2007). As MUSIC is employed to resolve ocean surface current structure (Schmidt, 1986), limitations in its performance are related to potentially suspect velocity outputs. Furthermore, different combinations of dynamic thresholds cutoffs have been analyzed to quantify the potential for error reduction (De Paolo et al., 2015). Since the question still remains open, further studies are currently underway to shed light on it.

In addition, the credibility of HF radar data has been previously tested in extensive validation studies, including direct comparisons of HF radar-derived surface currents against independent in situ sensors like moored ADCPs, point-wise current meters – PCMs hereinafter –, drifters or similar (Graber et al., 1997; Kaplan et al., 2005; Cosoli et al., 2010; Solabarrieta et al., 2014). Accordingly, a number of accuracy assessment exercises have been performed with the

HF coastal radar network operated by Puertos del Estado (Fig. 1a) – PdE hereinafter – in order to quantify and lower uncertainties in radar current measurements (Alfonso et al., 2006; Lorente et al., 2014, 2015a and b).

Correlation coefficients (CORR) and root mean squared error (RMSE) have been previously found to be in the ranges [0.32–0.92] and [6–30 cm s^{-1}], respectively (Kohut and Glenn, 2003; Paduan et al., 2006; Chapman and Graber, 1997). Relative HF radar velocity errors can vary dramatically with the radar transmission frequency, sensor type and location within the sampled domain, as well as the data processing scheme used (Rypina et al., 2014; Kirincich et al., 2012). In this framework, the instrumental noise and subgrid-scale current variability have been reported to yield noise levels of 4–6 cm s^{-1} (Emery et al., 2004; Ohlmann et al., 2007; De Paolo et al., 2015).

The main goal of this work is to explore basic features of the sea surface circulation in the Ebro River delta as derived from reliable and accurate HF radar surface current measurements. For this aim, a combined QC methodology is first applied: 1-year long real-time web monitoring of nonvelocity-based diagnostic parameters and offline validation of HF radar-derived current data with in situ observations from a PCM installed in a buoy moored within the radar domain (B1, Fig. 1b). This integrated approach is used during 2014 in order to infer both radar site status and HF radar system overall performance and also to provide upper bounds on both radial and total radar current measurement accuracy (Lorente et al., 2015c). Once HF radar data quality is estimated, Ebro delta HF radar capabilities in reproducing well-known circulation features are investigated through the exploration of monthly averaged flow patterns and dominant modes of variability both in time and space (Cosoli et al., 2012a and 2013; Kovačević et al., 2004). Lastly, the relative contribution of local wind as a forcing mechanism is evaluated.

This paper is organized as follows: Sects. 2 and 3 outline the specific instrumentation and methods used in this study, respectively, followed in Sect. 4 by a detailed discussion of the results. Finally, main conclusions are summarized in Sect. 5.

2 Instrumentation

2.1 HF radar

A CODAR SeaSonde standard-range HF radar system was deployed at the Ebro delta in December 2013 within the framework of the RIADE (Redes de Indicadores Ambientales del Delta del Ebro) project. The HF radar network consists of an array of three remote shore-based sites: Salou, Vinaroz and Alfacada. They will hereafter be referred to by their four letter site codes: SALO, VINA and ALFA, respectively (Fig. 1b).

The HF radar technology, founded on the principle of Bragg scattering of the electromagnetic radiation over a rough sea (Crombie, 1955), infers the radial current component from the Doppler shift of radio waves backscattered by surface gravity waves of half their electromagnetic wavelength. Each single radar site is configured to estimate radial currents moving toward or away from the receive antenna. Since the speed of the wave is easily derived from linear wave theory, the velocity of the underlying ocean surface currents can be computed by subtraction. The distance to the backscattered signal is determined by range-gating the returns and the angle of origin is inferred, in the case of CODAR SeaSonde radars, by a direction-finding process (Barrick and Lipa, 1986) using three collocated receive antennas (two orthogonal crossed loops and a single monopole) and the MUSIC algorithm (Schmidt, 1986).

Each site is operating at a nominal frequency of 13.5 MHz with a 90 KHz bandwidth, providing hourly radial measurements with a cut-off filter of 100 cm s^{-1} and representative of current velocities in the upper first meter of the water column. Only calibrated (measured) antenna beam patterns (hereinafter APMs) were employed by the software supplied by the manufacturer to process radial data used in the present study, with the aim of maximizing HF radar usefulness for operational applications (Lipa et al., 2006; Kohut and Glenn, 2003). In regions of overlapping coverage from two or more sites, radial current measurements are geometrically combined using a least-squares fit technique (Barrick and Lipa, 1986) with the averaging radius set to 6 km in order to estimate hourly averaged total current vectors on a predefined Cartesian regular grid with 3×3 km horizontal resolution. The maximum horizontal range is set to 80 km and the angular resolution is 5°.

HF radar-derived data used in this study were collected from 1 January to 31 December 2014 (Fig. 1c). During this period the three sites were simultaneously operational and radar coverage was as its maximum extent. Temporal data coverage was quantified by computing the percent of total possible vector returns at each radar grid point (Fig. 1b). Percent coverage decreases rapidly near the outer edges of the domain where error levels are higher due to poor intersecting beam geometry (Chapman and Graber, 1997) and quantified by larger geometric dilution of precision (GDOP, Chapman et al., 1997). GDOP is a unit-less coefficient of uncertainty that characterizes how radar geometry may impact on measurement accuracy and position determination errors, owing to the angle at which the radials intersect and also to uncertainties in the radial vectors geometrically combined (Levanon, 2000; Trujillo et al., 2004).

With the aim of screening out radar grid points where data are less reliable, a threshold on percent coverage has been imposed. Only time series of zonal and meridional surface currents at grid points with percent coverage greater than 50 % over the 2014 annual record have been considered in this

study. The selected coverage areas present associated GDOP values of 1.5 or less.

2.2 Buoy B1

The domain of the Ebro delta HF radar array includes an ocean Seawatch buoy deployed since August 2004 in the eastern waters of the Iberian Peninsula: Tarragona buoy (40.68° N, 1.47° E, 688 m depth), hereafter referred to as B1 (Fig. 1b). This buoy is equipped with an acoustic point-wise current meter manufactured by Falmouth Scientific Inc., providing quality-controlled hourly averaged current velocity vectors at a nominal depth of 3 m. A wind speed and direction sensor manufactured by R. M. Young Company measures hourly wind data at a nominal height of 3 m. It should be noted that current and wind records are only available from 1 May to 31 October 2014 (Fig. 1c). B1 suffered from brief communication outages during this period and subsequent short gaps (2–3 h) in data time series have been linearly interpolated.

3 Methods

3.1 Online quality control of HF radar measurements

In order to ensure the reliability of the HF radar products delivered, maintenance and quality control (QC) procedures must be performed at various stages on the data generation pipeline. The manufacturer software package integrates a set of QC routines and thresholding techniques in the data processing chain (e.g., limits for maximum vector magnitude and maximum GDOP).

This section presents a simplistic approach based on additional data quality checks at the post-processing stage and devoted to examining a variety of nonvelocity-based diagnostic parameters provided by the manufacturer (CODAR Ocean Sensors, COS) and listed in Table 1. Such indicators include hardware, antenna, radial and total parameters, employed here as diagnostic tools for evaluating HF radar integrity and health (Roarty et al., 2012; Emery and Washburn, 2007). A dedicated online website has been developed to operationally monitor in real time radar site status since anomalous values, inconsistencies or sharp fluctuations in the indicators might be related to potential malfunctions. This automated quality control web tool runs in background with a cron job, being updated on an hourly basis.

One-year long (2014) real-time monitoring has been performed in order to inspect the temporal evolution and consistency of the aforementioned parameters, obtain estimates of their standard ranges and evaluate Ebro delta radar site performance according to them (Lorente et al., 2015a). Abrupt or gradual degradation and failures can be easily detected, triggering alerts for troubleshooting when defined thresholds (initially set to 2 standard deviations above/below the mean) are persistently exceeded. Particular emphasis has been devoted to SNR3 and the number of radial vectors provided.

Finally, automated quality checks have been implemented at the second level within the hierarchy defined for QC procedures, referred to as total vectors. Temporal and spatial coverages of the Ebro delta radar system are separately analyzed on a monthly basis and later compared to each other to check whether HF radar systems operate within tolerance ranges, fulfilling the recommended level of data provision: 80 % of the spatial region over 80 % of the time (Roarty et al., 2012).

3.2 HF radar validation

Since the Ebro delta HF radar footprint overlooks a moored PCM within its spatial coverage, an accuracy assessment of radar surface currents is performed for a 6-month period May–October 2014 of concurrent radar–PCM measurements (Fig. 1c). The present section builds on previous investigations devoted to the determination of measurement errors, the evaluation of direction-finding capabilities and the angular distribution of radial velocity uncertainties (Emery et al., 2004; Paduan et al., 2006; Cosoli et al., 2010; De Paolo and Terrill, 2007).

For this aim, the radar radial arc geographically closest to the B1 buoy location has been selected for each HF radar site and radial current vectors estimated at each arc point have been compared with the radial projection of PCM velocities. The B1–HF radar comparative analysis allows the computation of statistical parameters (e.g., CORR and RMSE) as a function of the angle comprised between B1 and the arc grid point position. In the absence of direction-finding errors (DF), maximum CORR and minimum RMSE values should be found over the arc point closest to the B1 location. In the presence of DF, the bearing offset is thus expressed as the angular difference between the arc point with maximum correlation and the buoy location.

Radial current time series have been filtered to remove all tidal, diurnal and inertial fluctuations (the inertial period is 18.4 h at the B1 location latitude) from the velocity data. Filtered time series, obtained after applying a tenth-order digital low-pass Butterworth filter with a cut-off period of 30 h (Emery and Thomson, 2001), have been compared to evaluate the discrepancies in subinertial currents.

Complementarily, HF radar total vector hourly estimations at the grid point closest to the B1 location (HFR1; 1.48° E 40.69° N, Fig. 1b) have been compared with PCM velocities to provide upper bounds on the radar current measurement accuracy. Comparisons have been undertaken using zonal (U) and meridional (V) components in order to evaluate the agreement between both instruments by means of the computation of a set of statistical metrics – RMSE, scalar and complex correlations and best linear fit of scatterplots. Monthly results have been summarized with Taylor diagrams (Taylor, 2001), which provide a concise statistical summary of the agreement between both data sets.

Table 1. Diagnosed parameters used to operationally monitor Ebro delta HF radar status in real time. The HF radar system's performance is routinely evaluated through the analysis of the indicators listed below at different frequencies (daily/weekly/monthly).

Site status		
Type	Parameter	Description
Receiver	MTMP, RTMP	Chassis and board temperatures.
Transmitter	XPHT, XAHT	Chassis and amplifier temperatures.
Transmitter	XAFW, XARW	Forward and reflected powers.
Antenna	SNR1, SNR2, SNR3	Signal-to-noise ratio at loop 1, loop 2 and the monopole.
Antenna	AMP1, AMP2	Calculated amplitude corrections for loops 1 and 2 to the monopole.
Radial	Number radials/u.t., range and bearing	Abrupt decrease can be related to a potential malfunction.
System status		
Parameter		Description
Temporal coverage		Data availability (%): areas of poor data return (< 50 %) are discarded from any analysis.
Evolution of spatial coverage		Monitoring of fluctuations due to the day–night cycle. Identification of time steps of sharp decrease in spatial coverage.
Spatial coverage vs. temporal coverage		Verification of the 80–80 % recommended level of data provision.
COS uncertainty metrics (standard deviation of U/V, covariance U/V)		Useful resource, based on fluctuations in the data themselves.

Finally, rotatory spectral analyses (Gonella, 1972) have been performed for HF radar-derived total vectors at the HFR1 location and for current data from B1 in order to identify the dominant modes of temporal variability. To ensure the continuity of the data record, small gaps detected (not larger than 6 h) in time series have been linearly interpolated. Spectra have been calculated by dividing time series into successive 6-day segments, with a 50 % overlap and a Hanning window (Emery and Thompson, 2001), and subsequently averaged to provide some smoothing. Confidence levels for spectra densities have been derived assuming a chi-squared distribution for the variance.

3.3 Characterization of the surface circulation field

Maps of the Eulerian mean current field have been constructed at a monthly timescale from the raw (unfiltered) radar time series on a subsampled grid with the aim of assessing the surface current dynamics in the Ebro delta. Additionally, a complex empirical orthogonal function (EOF) decomposition (Kundu and Allen, 1976) has been used to infer the driving forces and spatiotemporal scales behind the variability of sea surface currents (Kaihatu et al., 1998). This method, which reduces the components of the vector field to a complex scalar, has become widespread in order to extract the dominant modes of variability. The representative spatial patterns (or EOF modes) and their corresponding temporal coefficients or principal components (PCs, which describe the evolution of the modes) are determined by using the singular value decomposition of the covariance matrix. Each statistically significant EOF mode explains a limited portion of the total surface current variance.

EOF analysis has been applied to the radar current velocity data set using again the raw (unfiltered) hourly time series for the entire year of 2014. The main spatial modes obtained for HF radar have been interpreted in terms of physical processes related to the detected spatially coherent structures. Since EOFs are purely statistical, each EOF mode's statistical significance must be evaluated. Several rules of thumb have been previously proposed, indicating when an EOF is likely to be subject to large sampling fluctuations. In the present work, error estimates based on temporal decor-

relation scales have been calculated according to North et al. (1982):

$$\delta(\lambda_i) = \lambda_i \cdot (2/N)^{\frac{1}{2}}, \quad (1)$$

where δ_i is the eigenvalue for mode i, and N is the number of degrees of freedom determined using a conservative 2-day decorrelation timescale, following Münchow and Chant (2000). If the confidence intervals from the error estimates of any modes overlap, the modes may be non-orthogonal and can not be considered distinct and uncorrelated. Consequently, such modes are excluded from the EOF analysis and hence only the first previous modes can be considered to contain a significant portion of the total variance and to properly reproduce the observed surface current fields.

Finally, the hourly wind vector data set registered at the B1 buoy has been decomposed into principal components in order to infer the main axis of variability. Particular emphasis has been placed on the relationship between wind and radar-derived current EOF modes of variability in order to derive a better statistical insight.

4 Results and discussion

4.1 Annual quality control

Boxplots of SNR3 for each radar site (Fig. 2a, b, c) exhibit a consistent monthly evolution, with a median (central mark) above 40 dB. However, a number of sharp decreases can occasionally be observed at the VINA site for the month of June (Fig. 2c), exceeding the previously reported threshold of 10 dB (De Paolo and Terril, 2007).

The annual time series of hourly SNR3 values for the VINA site (Fig. 2d) reveals that the thresholds proposed in the present work (2 standard deviations above/below the mean, represented by bold blue dotted lines) were abruptly exceeded several times in June. SNR3 reached extremely low values, leading to a drastic reduction in the radar spatial coverage presumably related to an inherent limitation of the MUSIC algorithm, namely, the extraction of a maximum of two bearing solutions for a given range cell and a given radial current velocity. In this context, poor SNR3 values associated with potential interferences or environmental noise can lead to ambiguities in the estimation of the direction of arrival (DOA) function performed by the MUSIC algorithm. Such ambiguities, based on the existence of more than two bearing solutions, eventually produce gaps in HF radar spatial coverage since additional solutions are excluded.

Consequently, the number of radial vectors (NRV) provided by VINA decreased significantly in June (Fig. 2e). Leaving aside the regular high-frequency fluctuations due to the day–night cycle, NRV was several times below 500 and even equal to zero, indicating a poorer than expected performance of the VINA site during this month. Nonetheless, it appears to be a sporadic episode, maybe related to radio-

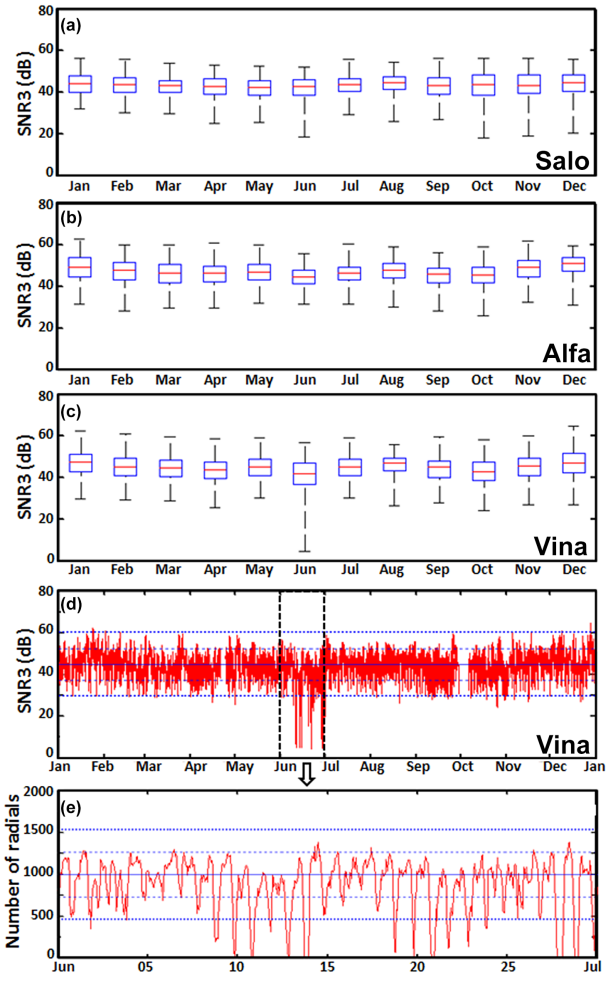

Figure 2. Annual quality control of Ebro delta radar sites, SALO **(a)**, ALFA **(b)** and VINA **(c)**, based on monthly boxplots of the signal-to-noise ratio at the monopole (SNR3) for 2014. In each box, the central mark is the median, the edges of the box are the 25th and 75th percentiles, and the whiskers extend to the most extreme data points. **(d)** Annual time series of hourly SNR3 values for the VINA site. **(e)** Monthly time series of hourly radial vectors provided by the VINA site during June 2014. The solid and dashed blue lines represent the mean and the standard deviation for the entire 2014, respectively. The bold blue dotted lines denote the thresholds of 2 standard deviations above/below the mean.

wave interferences, since VINA presented a stable performance during the second semester of 2014.

The quality checks implemented at the total vector level allow an overall evaluation of Ebro delta HF radar system performance on a monthly basis (Fig. 3). A comparative analysis for February and June confirms the degraded performance during the latter. Data availability generally exceeded 80 % in time over the majority of the radar footprint in February, with an abrupt decrease at the periphery of the radar range (Fig. 3a). By contrast, it only outreached 50 % in June, with a smoother transition at the outer edges of the domain

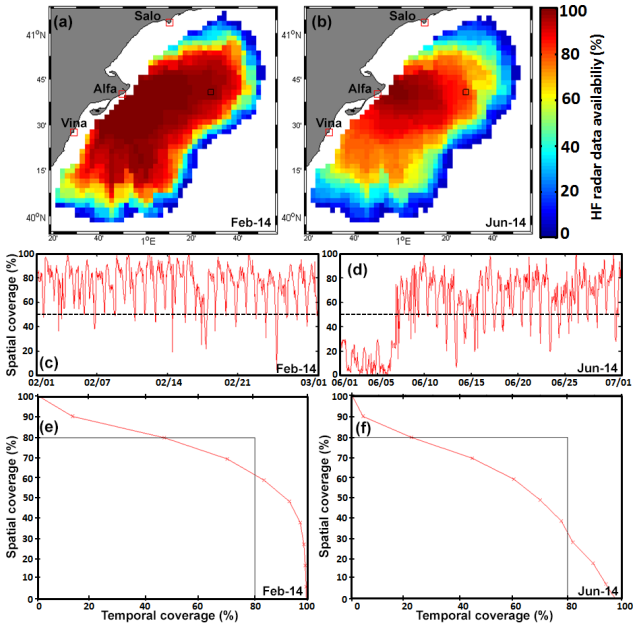

Figure 3. Evaluation of Ebro delta HF radar system performance on a monthly basis: February (left) and June (right) 2014. A comparative analysis is carried out for the radar data availability **(a–b)**, the temporal evolution of the spatial coverage **(c–d)** and the relationship between both the spatial and temporal coverage **(e–f)**. The black square represented in **(a–b)** denotes the B1 buoy location.

(Fig. 3b). The evolution of the spatial coverage was rather consistent in February, with sporadic decreases below 50 % (Fig. 3c). On the contrary, an irregular performance is detected in June as a consequence of both ALFA site outage (1–8 June) and VINA irregular behavior (Fig. 3d). The first factor yielded a dramatic and persistent drop in the areal coverage, lower than 20 % most of the time. The second led to a significant, albeit occasional, reduction in the radar spatial domain (below 50 %), which can be observed from 8 to 30 June 2014.

Finally, the temporal and spatial coverages have been compared to each other (Fig. 3e, f). The Ebro delta radar system was closer to fulfilling the required 80–80 % level of data provision in February (Roarty et al., 2012), with 64 % of the areal domain (referred to as its maximum extent) available 80 % of the time. By contrast, the radar system barely reached 35 % of spatial coverage for 80 % of the time in June. Despite this occasional degradation, radar sites' overall performance and their day-to-day operation have been found to be robust and within tolerance ranges. One year of continuous operation revealed three sites up and operational in excess of 95 % of the time, with sporadic interruptions that introduced short-duration gaps in time and space (Fig. 1c).

It is noteworthy that the described methodology, at this preliminary development stage, is not able to remove suspicious values or outliers from the data stream in real time like Cosoli et al. (2012b), but only to detect anomalies and categorize them in order to create a historic database of flagged radial files similar to Roarty et al. (2012) for a later offline reprocessing of total vector maps when one (or more) radar site(s) is (are) considered to be working abnormally. In this context, the hourly radial vectors provided by the VINA site in June that did not satisfy the proposed QC control have been discarded from the analyses performed in the next sections and the associated total vector maps have been accordingly reprocessed offline. Future efforts should be devoted to improving radial data quality in real time prior to the vector combination process and also to assigning meaningful quality descriptor flags for all grid point data in total current fields.

4.2 Buoy–radar comparison results

The evaluation of direction-finding capabilities revealed the existence of small bearing errors (hereafter $\Delta\alpha$) in radar radial estimations, ranging between 2 and 8° (Fig. 4) and in accordance with the typical values previously reported (Emery et al., 2004; Paduan et al., 2006). Comparison of unfiltered hourly radial currents estimated by B1 and the SALO site (Fig. 4b) shows maximum CORR in a grid point (denoted by a vertical solid red line) angularly close to the B1 location (vertical dotted black line): 0.79, with an associated RMSE of 10.95 cm s^{-1} and $\Delta\alpha$ of 3.74° in the counter-clockwise direction. The VINA site (Fig. 4c) presents a lower bearing offset ($\Delta\alpha = 1.82°$) but also a lower (higher) CORR (RMSE) value of 0.58 (13.31 cm s^{-1}). It is worth mentioning that minimum RMSE values are also located in the vicinity of the correlation peaks. The VINA site exhibits the largest pointing error ($\Delta\alpha = 7.82°$) and the poorest agreement with moored radial estimations as CORR is 0.58 and RMSE is fairly above 18 cm s^{-1} (Fig. 4d).

Hourly time series of low-pass filtered radial currents measured by B1 and those estimated in the closest range arc point ("best match-angle") by each HF radar site are presented in Fig. 5. Metrics derived from the accuracy assessment highlight the consistently high agreement between the SALO radar site and B1 estimations, with CORR and RMSE values of 0.80 and 5.58 cm s^{-1}, respectively (Fig. 5a). Results derived from the best linear fit reveal a slope close to 1 and an intercept up to -0.82 cm s^{-1}. The concordance between the ALFA site and B1 is moderately good, with acceptable pairs of values CORR–RMSE and slope intercept: [0.63–6.91] and [0.73–1.92] cm s^{-1}, respectively (Fig. 5b). VINA site data show lower agreement with in situ measurements (Fig. 5c), as reflected by a lower (higher) CORR (RMSE) value of 0.56 (7.76 cm s^{-1}). This might be partially attributable to the long site–buoy distance (i.e., the radar signal is weaker) and to the limited radar data availability due to day/night coverage fluctuations (i.e., the data return is more than 3 times lower, with only 986 hourly observations available).

Ancillary validation works with radial measurements like internal self-consistency checks have not been performed due

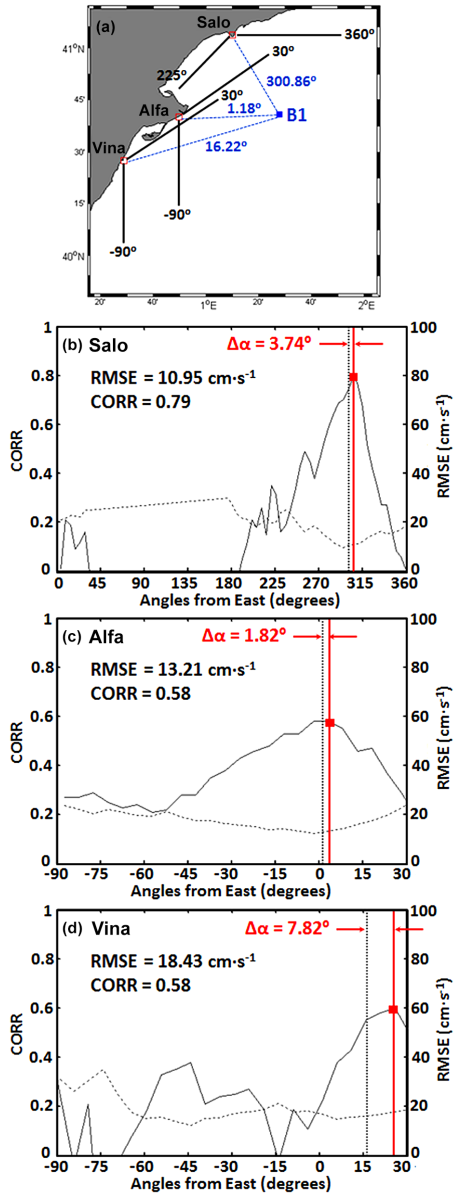

Figure 4. (a) Angular position of Ebro delta HF radar sites with respect to the B1 buoy location. Angle values are measured counterclockwise from east, indicating arc limits and buoy direction. **(b–d)** Correlation (solid line) and RMSE (dashed line) between unfiltered radial currents estimated by the B1 buoy and those measured by three HF radar sites, SALO **(b)**, ALFA **(c)**, and VINA **(d)**, using calibrated antenna patterns for a 6-month period May–October 2014. The vertical dotted line represents the angular position of B1. The vertical red solid line denotes the angular position of maximum correlation (CORR), which is gathered with the associated RMSE and bearing offset ($\Delta\alpha$) values.

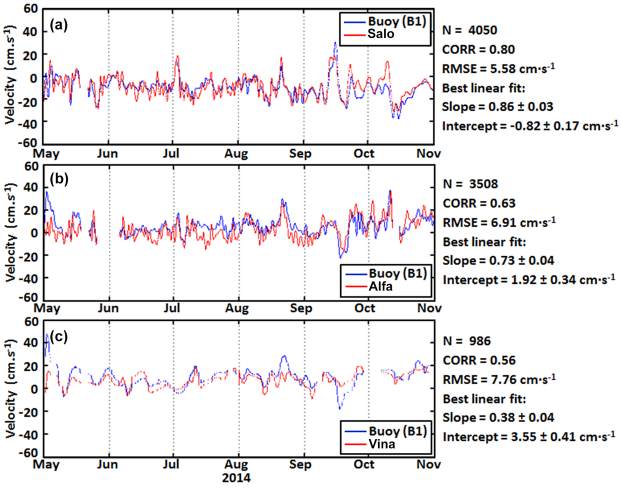

Figure 5. Comparison of low-pass filtered hourly time series (cut-off period of 30 h) of radial currents measured by B1 buoy (blue line) and HF radar sites (red lines): **(a)** SALO, **(b)** ALFA and **(c)** VINA in the range arc point closest to the B1 location for a 6-month period May–October 2014, using calibrated antenna patterns. *N*, slope and intercept represent the number of hourly radial current observations and the results derived from the best linear fits, respectively.

to the Ebro delta radar sites' geometry. Radar-to-radar comparisons along the overwater baselines (Paduan et al., 2006; Yoshikawa et al., 2006; Atwater and Heron, 2010), although valuable for exploring quantitatively intrinsic uncertainties in radial velocities, are not feasible since they are positioned over land or near the coastline.

Statistical metrics derived from filtered hourly time series comparison of zonal (U) and meridional (V) components of total vectors estimated by B1 and HFR1 for the 6-month period are presented in Fig. 6. Results reveal a good agreement for both components (CORR above 0.74), in accordance with results reported in the literature (Cosoli et al., 2010; Kaplan et al., 2005). RMSE is significantly higher for the zonal component than for the meridional: 12.69 vs. 4.02 cm s^{-1} (Fig. 6a, b). The disparity of uncertainty levels between the east and north component vectors comes for the geometry of the radar vector combination and the prevalent south-southwestward current flow. This presumably might lead to less (more) precise radial vectors provided by the ALFA (SALO) radar site since radial measurements have proven to be more accurate when the dominant current flow moves in the same direction (Robinson et al., 2011). Since the ALFA (SALO) site contributed mainly to the HF radar zonal (meridional) current assessment in the nearby B1 region, a strong relationship between radial and total vector uncertainties has been shown.

The scatterplots (not shown) and the associated best linear fits show that HF radar slightly underestimates total current velocities registered by B1 since the slopes are below 1: 0.71 and 0.67 for U and V components, respectively. The time-averaged complex correlation coefficient between B1 and HFR1 currents at zero lag is 0.77. The related phase is 8.65°, indicating that the former are, on average, slightly right

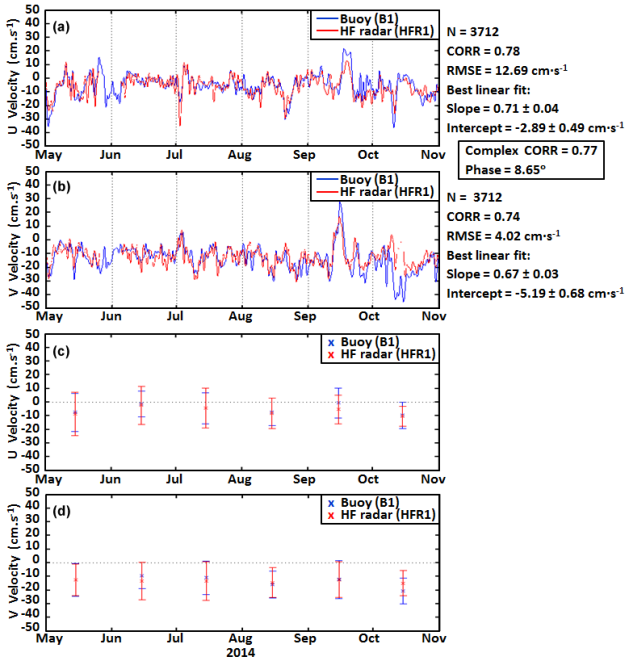

Figure 6. Low-pass filtered (cut-off period of 30 h) hourly time series of zonal **(a)** and meridional **(b)** components of total currents measured by the B1 buoy (blue line) and HF radar at the closest grid point HFR1 (red line), for a 6-month period May–October 2014. Mean zonal **(c)** and meridional **(d)** current velocities, averaged over individual months for both HF radar and B1 measurements, with 1 standard deviation (error bars represent the 95 % confidence interval).

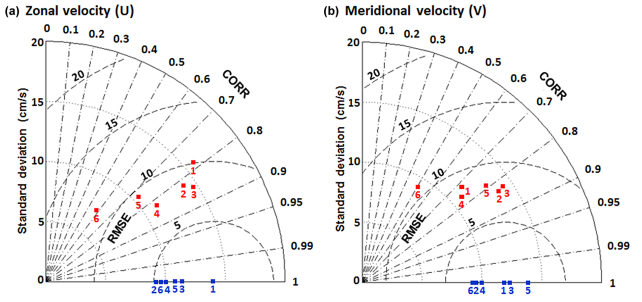

Figure 7. Taylor diagrams, based on the law of cosines, provide a concise statistical summary of how closely unfiltered hourly radar estimations (red filled squares) match with B1 observations (blue filled squares), considered here as the reference points of perfect agreement. Taylor diagrams for zonal **(a)** and meridional **(b)** velocity components gather the monthly statistical metrics derived from HF radar–B1 comparison. Sequential numbers refer to individual months of the analyzed period May–October 2014 (1: May; 6: October).

shifted since the veering angle gives the average counterclockwise turning of the second vector with respect to the first vector (Kundu, 1976).

The monthly mean current values were computed to characterize the main features of the flow in this region. The descriptive statistics reveal predominant negative values for the zonal speed (Fig. 6c) and a quasi-permanent average flow in the N–S direction (Fig. 6d). There is no evidence of a seasonal signal in both zonal and meridional velocity components of radar and B1 surface currents. Therefore, both instruments exhibit similar monthly mean values and variability, capturing the well-known southwestward thermohaline flow and identifying episodic but intense current reversals, such as those observed by mid-September (Fig. 6a, b).

The monthly comparison of total vectors, performed on the unfiltered time series, provides a variety of metrics that are concisely summarized in a Taylor diagram (Taylor, 2001) shown in Fig. 7. The diagram compares both data sets by combining information about their relative standard deviations, centered RMSE and CORR, synthesizing the statistical information of how closely the radar measurements at the HFR1 grid point match with B1 velocities. As can be seen, the cluster of points that show the best agreement (i.e., are closest to their corresponding reference point, labeled with blue squares) are those corresponding to the period May–September (red squares, sequentially numbered 1–5). The reported correlation coefficient, standard deviation and RMSE values emerge in the ranges of [0.72–0.83], [10.96–14.18] and [7.48–8.75 cm s^{-1}], respectively, for both zonal and meridional velocity components (Fig. 7a, b). However, HF radar is less accurate by the last month of the analyzed period, since metrics computed for October (red square 6) reflect lower (higher) CORR (RMSE) values: 0.50–0.58 (10.92–11.03).

Instrument-to-instrument comparisons present intrinsic limitations since both devices operate differently and at distinct nominal depths. A fraction of observed radar–B1 differences can thus be explained in terms of different sampling strategies on disparate timescales and space scales (Ohlmann et al., 2007). In this context, many of the uncertainties associated with HF radar technology are geometric in nature. Apart from the instrumental noise, other sources of potential errors in vector currents might be the sub-grid horizontal shear, the geophysical variability within the water column (Graber et al., 1997) and some specific processes, namely, the Stokes drift, the Ekman drift and baroclinity (Paduan et al., 2006).

Spectral analyses have been computed for the 6-month period May–October 2014 (warm stratified season) to examine power spectral discrepancies in the frequency domain between both instruments. B1 and HFR1 current time series present qualitatively similar characteristics, capturing properly the dominant features within the diurnal and inertial bands, related to significantly prevalent clockwise (CW) rotatory motions (solid lines, Fig. 8). Relevant polarized peaks are evident for both data sets, although their amplitudes are slightly larger for radar currents (solid red line). The inertial peak is the most pronounced, pointing out the adjustment of the stratified fluid to the wind-driven currents and, sub-

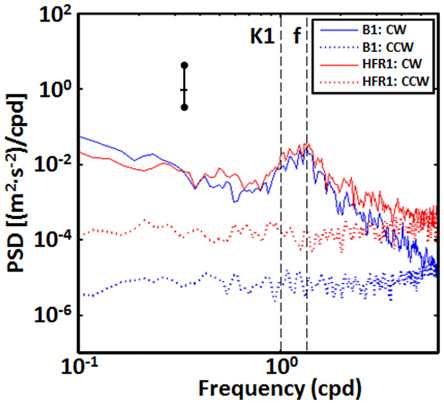

Figure 8. Spectral density of the rotary auto-spectra of the B1 buoy (blue) and HF radar at the closest grid point HFR1 (red), performed for a 6-month period May–October 2014 of concurrent records. Clockwise (counter-clockwise) components are represented by solid (dotted) lines. Vertical dashed lines indicate the frequencies of the diurnal constituent (K_1) and the inertial oscillations **(f)**. Error bars indicate the 95 % confidence interval.

sequently, the importance of local wind as a forcing mechanism (addressed in Sect. 4.3.2). Offshore oscillations in this frequency band are a common feature in ocean circulation and their presence in the study area has been previously documented (Font et al., 1990). By contrast, the counter-clockwise component (CCW, dotted lines) is much less energetic (especially in the case of B1 current estimations) and is where the main radar–B1 differences in variance distribution can be found. Finally, a drop of energy and later flattening about 2 cpd are common for the CW components of both B1 and radar spectra, although the latter presents larger energy at that frequency band. Radar surface estimations are influenced by energetic high-frequency processes related to air–sea interaction like highly variable and strong wind gusts, which are not fully contained in sub-surface current estimations provided by the current meter.

4.3 Dominant features of the surface flow

4.3.1 Monthly averaged current patterns

The sequence of monthly averaged current maps in Fig. 9 shows that some of the main circulation features in the Ebro delta remain rather invariant throughout most of the year, like the southwestward slope jet, associated with the highest velocities detected (above 30 cm s^{-1}). The current speed diminishes toward coastal areas, except in the vicinity of the ALFA radar site, where the signal of Ebro River impulsive-type freshwater outflow is clearly evidenced during winter and spring (Fig. 9a, b, f). As a consequence of the remarkable seasonal variability of Ebro discharge rates, the river plume loses intensity during the warm season (Fig. 9c), becoming barely noticeable in late summer and early fall

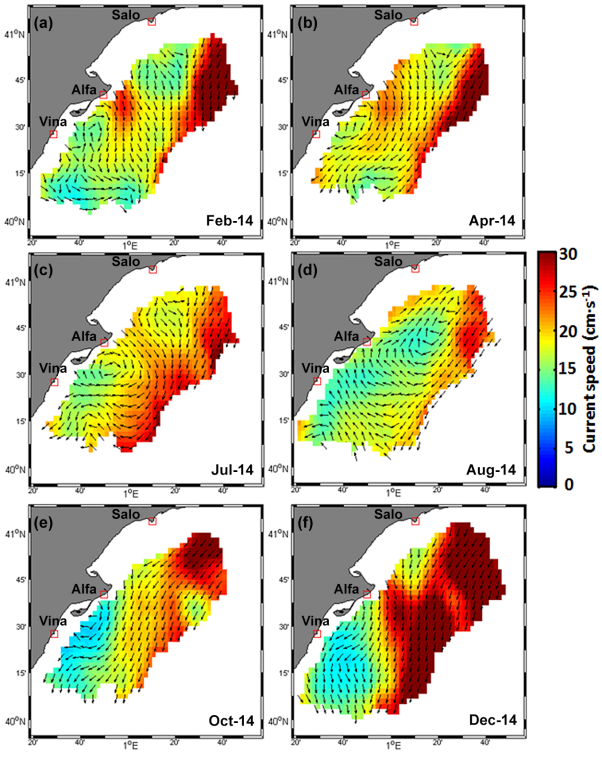

Figure 9. Monthly averaged surface velocity fields, based on unfiltered hourly HF radar current data, for **(a)** February, **(b)** April, **(c)** July, **(d)** August, **(e)** October, and **(f)** December 2014. The study area is not uniformly covered since only radar grid points satisfying a minimum data return of 50 % over the monthly record have been considered. Only one grid point of every two is plotted for visualization reasons.

(Fig. 9d, e), until the beginning of the following hydrological cycle (Fig. 9f).

The weakening of the southwestward slope jet during the central part of the year is noteworthy, in agreement with reported short periods of current reversals (Font et al., 1990). The jet is intensified in October, perhaps as a result of the observed increase in the mesoscale activity (Font et al., 1995), reaching ultimately a peak strength in December. By the end of 2014, the monthly spatial patterns become rather uniform, revealing the acceleration of the jet (with a spatial propagation of maximum velocities, exceeding 40 cm s^{-1}) in the eastern region of the radar domain and also the presence of two small-scale coastal meanders (Fig. 9e, f).

A coastal anticyclonic eddy can also be observed in radar data, confined to south of the Ebro delta mouth (Fig. 9a, b, c). This hydrodynamic feature has been well documented in previous studies (Font et al., 1990; Salat et al., 2002), which stated the interaction of the buoyancy-driven flow with the topography as the triggering source of this clockwise gyre, eventually reinforcing the shelf-slope front that drives the general circulation to the south-southwest. In addition, persistent and high-intensity northwesterly wind jets (called

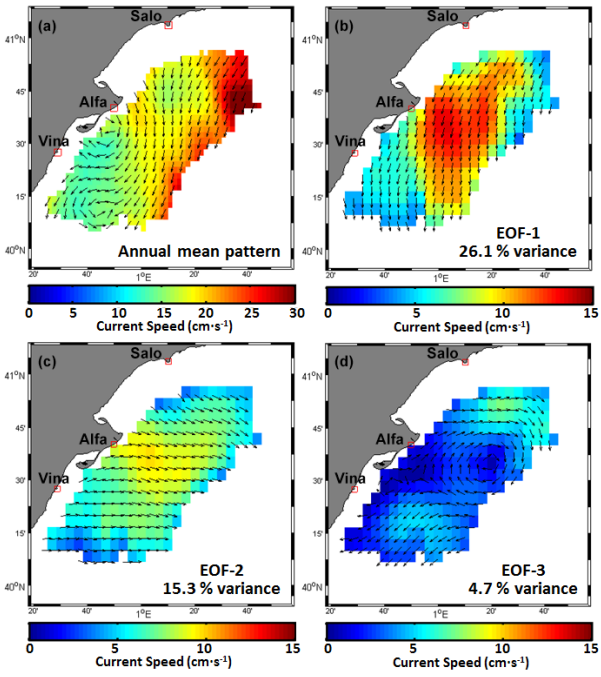

Figure 10. Spatial patterns of the **(a)** annual mean velocity field and **(b)** first, **(c)** second and **(d)** third EOF dominant modes of unfiltered hourly radar surface currents for 2014. Current vectors were plotted in every second grid point for clarity. Variance explained is indicated in the lower right corner of the corresponding panel.

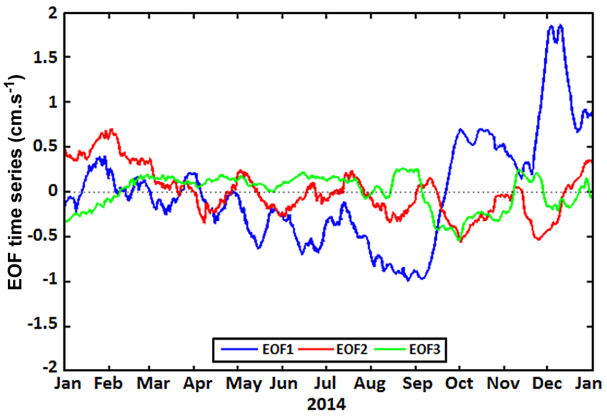

Figure 11. Time coefficients of the first (blue), second (red) and third (green) EOF modes of the hourly radar current data set evaluated for the entire year 2014. Time series have been filtered with a 20-day running mean.

"mistral" winds), dominant during the October–May cold season and channeled by the narrow Ebro Valley, have been reported to introduce negative vorticity in the flow south of the Ebro delta and to reinforce the long-term preservation of this small-scale eddy (Garcia and Ballester, 1984; Espino et al., 1998). Notwithstanding, this coastal clockwise rotation is eventually absent from September (not shown) to December monthly averaged current maps.

During the transition month of August, a large anticyclonic recirculation cell is evidenced, detached from the shore and located in the center of the radar domain (Fig. 9d). This current pattern is dominated by the interaction of the cross-shelf flow on the southern inner shelf with topographic obstacles, giving rise to a shift to the right of the coastal flow. The subsequent northeastward reversal of the inshore flow is scarcely influenced by Ebro River freshwater discharge as it reaches the lowest value at this stage of the year.

4.3.2 Empirical orthogonal function (EOF) analysis

The mean and EOFs of hourly surface currents have been calculated for the entire 2014 (Fig. 10). The long-term mean flow (Fig. 10a) captures the main circulation features previously reported about the North Current, characterized by a quasi-permanent shelf-slope jet oriented southwestward and a remarkable Ebro River impulsive-type freshwater discharge (located in front of the ALFA site). The buoyancy input introduced by large delta outflows, together with topographic effects, leads to the development of the aforementioned anticyclonic coastal eddy on the southern side of the delta.

Since the EOF analysis has been performed on the unfiltered data set containing relevant high-frequency spatiotemporal variability, the first three EOFs cumulatively account only for 46.1 % of the total variance (26.1, 15.3 and 4.7 %, respectively). Only the first three EOF modes are statistically significant according to the mode selection rule and truncation criterion suggested by North et al. (1982). The first, second and third modes are distinct and uncorrelated; however, the fourth mode is not since its error bars overlap with those of mode 5 (not shown). Therefore, higher-order modes will not be further addressed here as they represent a combination of unresolved high-frequency motions or noise (Cosoli et al., 2012a).

The first dominant EOF mode (Fig. 10b) represents a spatially uniform pattern, rather similar to the annual averaged current map, with a prevailing alongshore shelf-slope jet flowing mainly southwestward, basically capturing the thermohaline Catalan front. The second EOF (Fig. 10c) shows a homogeneous spatial structure, perpendicular to the first mode, with a well-defined offshore-directed flow. The spatial pattern of EOF3 (Fig. 10d) adds some complexity to the basic uniform flows represented by the first two modes, since it introduces curvature to the current field by means of a large, albeit weak, anticyclonic recirculation cell (flow divergence) in the central (southern) region of the radar domain.

Temporal variation in the strength of these three EOF modes is represented by their corresponding principal components shown in Fig. 11. EOF1 is predominantly positive except during the summertime, when the quasi-permanent flow to the SW is altered by clockwise inertial oscillations

(positive EOF3) and some periods of current reversals, with maximum occurrence during the stratified warm season as reported by Font et al. (1990). Nevertheless, EOF1 becomes strongly positive again during the fall, reaching a peak by mid-December, in clear agreement with the strengthened shelf-slope jet flowing southwestwards shown in Fig. 9f. The temporal structure of EOF2 reveals a principal offshore-directed flow through the January–May period and also in late December, coincident with the cold season (October–May) that is characterized by both energetic mistral winds and Ebro River high discharge rates. Lastly, EOF3 adds clockwise curvature for most parts of the year (February–September and November). The evident enhancement of the anticyclonic gyre in August (positive EOF3), combined with the onshore-directed flow (negative EOF2) and the reversal of the main current flow (negative EOF1) during that time period, gave rise to a complex circulation scheme rather similar to the monthly averaged pattern represented in Fig. 9d.

In order to define the prevalent wind directions registered at B1, the major and minor variance axes have been determined (Fig. 12a). The results show that the main variability occurs along a direction 99° azimuth containing 54 % of the total energy. This is the EOF1 mode, largely aligned with persistent and intense northwesterly mistral winds channeled by the narrow Ebro Valley (Font, 1990). The orthogonal EOF2 mode is oriented 9° clockwise from north and holds the remaining 46 % of the variance, capturing mainly the influence of alongshore winds.

Linear correlation coefficients have been computed between the principal components related to the two main wind EOF modes of variability and radar-derived EOF2, since the cross-shelf circulation shown in Fig. 10c might be presumably driven by strong local winds. The high correlation between the filtered principal components can be readily seen in Fig. 12b–c, with a value of 0.47 (0.67) for wind-PC1 (PC2) and radar-PC2, respectively. The results underline that the surface current variability in the Ebro delta can be influenced by wind action, in accordance with Espino et al. (1998), who demonstrated such a relationship when winds are strong and steady enough. The higher agreement between both wind–radar PC2 appears to be consistent with Ekman transport to the right of the wind direction. By contrast, northwesterly mistral wind events (PC1) are expected to enforce the prevalent offshore-directed circulation regime (radar EOF2) by increasing the mean speed of the flow.

Equally, the influence of local wind forcing on HF radar EOF1 mode has been assessed (but not shown), with a correlation coefficient of 0.52 (−0.28) for wind PC1 (PC2). This finding highlights the impact of mistral winds on the predominant southwestward flow, by inducing an Ekman veering.

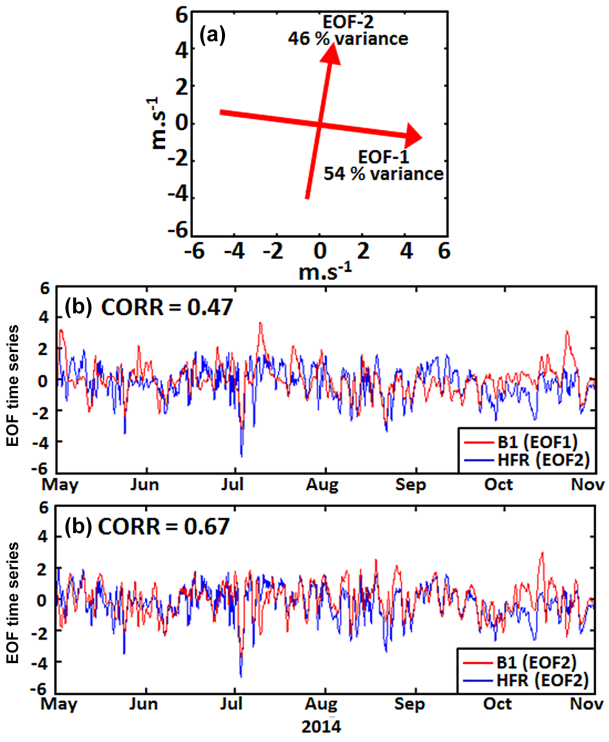

Figure 12. (a) Main axes of variability for hourly wind data registered at the B1 buoy. **(b)** Principal components of the first EOF mode of wind ($m\,s^{-1}$, in red) and the second EOF mode of radar currents ($cm\,s^{-1}$, in blue). **(c)** Principal components of the second EOF mode of wind (red) and the second EOF mode of radar currents (blue). The amplitudes have been normalized by their respective standard deviations and filtered with a 1-day running mean.

5 Concluding remarks and future work

Since the acquisition of high-quality surface current data remains a priority for HF radar operators and the research community, a combined quality control (QC) methodology has been applied for a three-site standard range (13.5 MHz) CODAR SeaSonde HF radar network deployed at the Ebro delta (northeastern Spain). This integrated approach consists of 1-year long (2014) real-time web monitoring of nonvelocity-based diagnostic parameters, coordinated with a 6-month (May–October 2014) validation of HF radar data (at both the radial and total vector levels) with independent in situ observations from a point-wise current meter installed in the B1 buoy, moored within the radar footprint.

The overall stable and accurate performance of Ebro delta HF radar during 2014, derived from the combined QC-validation approach, suggests that sites were functioning properly and that their APMs were correctly performed and integrated in the data processing. This provides ground truth to examine future radar performances.

The analysis of the monthly averaged spatial patterns of the velocity field shows that the HF radar properly represents basic oceanographic features and recurrent circulation patterns previously observed in the study area, namely, the predominant southwestward flow, the coastal clockwise eddy confined to south of the Ebro delta mouth or the Ebro River

impulsive-type freshwater discharge. It is also noteworthy that this study has been performed in a low-energy shelf where the surface currents are generally weaker than most of those referenced herein (Lorente et al., 2014). The EOF analysis related the flow response to local winds and confirmed that the surface current field evolved in space and time according to three dominant modes of variability, which significantly account for 46.1 % of the variance.

Regarding the Ebro delta study area, active and planned efforts are devoted to an extensive description of a variety of marine processes impacting on the evolution and reshape of the nearshore deltaic area: the wave action eroding exposed wetlands, the sediment transport, the freshwater discharges and buoyancy fluxes (which further complicate water motions in the Ebro delta) and ultimately the major influence of local wind forcing.

Future works should include the use of verified HF radar data for the rigorous skill assessment of operational ocean circulation systems currently running in the Ebro delta region, like the IBI (Iberia–Biscay–Ireland) regional system (Sotillo et al., 2015), implemented within the framework of MyOcean projects and the Copernicus Marine Environment Monitoring Service (CMEMS). A combined observational and modeling approach would provide a comprehensive characterization of the coastal circulation and benefit from the complementary nature of both systems. HF radar observations improve the model description by resolving low-scale processes in areas with significant topographic gradients, whereas model outputs provide a 3-D quantitative picture with vertical resolution that completes the surface radar-derived information when the quality data or the spatiotemporal coverage are poorer.

This integrated strategy might complement and optimize the intense monitoring activity performed around the deltaic coastline through the timely and seamless delivery of high-quality operational products, devoted to supporting wise decision-making and mitigating anthropogenic hazards in the marine environment. Such products could also provide paramount information on biological connectivity between the Ebro delta marine protected area and other relevant ecological regions in the western Mediterranean Sea.

Acknowledgements. The authors gratefully acknowledge the Qualitas Remos Company (a partner of CODAR Ocean Sensors) for the useful suggestions, and deeply appreciate comments provided during the paper revision process by Donald Barrick, Jeffrey Paduan and Guillaume Charria, which significantly improved the quality of the manuscript. The Spanish Ministerio de Economía y Competitividad supported this study through the OPErational RAdars for research in marine sciences (OPERA) project (CTM2012-33223).

Edited by: P.-Y. Le Traon

References

Alfonso, M., Álvarez-Fanjul, E., and López, J. D.: Comparison of CODAR SeaSonde HF Radar operational waves and currents measurements with Puertos del Estado buoys, Final Internal Report of Puertos del Estado, 1–32, 2006.

Atwater, D. P. and Heron, M. L.: HF radar two-station baseline bisector comparisons of radial components, Proceedings of IEEE Oceans 2010, Sydney, Australia, 1–4, 2010.

Atwater, D. P. and Heron, M. L.: A first approach to SeaSonde quality control, Proceedings of IEEE Oceans 2011, Waikoloa, HI, USA, 1–5, 2011.

Barrick, D. E. and Lipa, B. J.: Correcting for distorted antenna patterns in CODAR ocean surface measurements, IEEE J. Oceanic Eng., OE-11, 304–309, 1986.

Barrick, D., Fernandez, V., Ferrer, M. I., Whelan, C., and Breivik, Ø.: A short-term predictive system for surface currents from a rapidly deployed coastal HF radar network, Ocean Dynam., 62, 725–740, 2012.

Chapman, R. D. and Graber, H. C.: Validation of HF radar measurements, Oceanography, 10, 76–79, 1997.

Chapman, R. D., Shay, L. K., Graber, H. C., Edson, J. B., Karachintsev, A., Trump, C. L., and Ross, D. B.: On the accuracy of HF radar surface current measurements: intercomparison with ship-based sensors, J. Geophys. Res. 102, 18737–18748, 1997.

Codar Ocean Sensors: SeaSonde Diagnostic Files, CODAR Internal Document, May, 2005.

Cosoli, S., Mazzoldi, A., and Gacic, M.: Validation of surface current measurements in the Northern Adriatic Sea from High Frequency radars, J. Atmos. Ocean. Tech., 27, 908–919, 2010.

Cosoli, S., Gacic, M., and Mazzoldi, A.: Surface current variability and wind influence in the north eastern Adriatic Sea as observed from high-frequency (HF) radar measurements, Cont. Shelf Res., 33, 1–13, 2012a.

Cosoli, S., Bolzon, G., and Mazzoldi, A.: A Real-Time and Offline Quality Control Methodology for SeaSonde High-Frequency Radar Currents, J. Atmos. Ocean. Tech., 29, 1313–1328, 2012b.

Cosoli, S., Licer, M., Vodopivec, M., and Malacic, V.: Surface circulation in the Gulf of Trieste (northern Adriatic Sea) from radar, model, and ADCP comparisons, J. Geophys. Res., 118, 6183–6200, 2013.

Crombie, D. D.: Doppler spectrum of sea echo at 13.56 Mc/s, Nature, 175, 681–682, 1955.

De Paolo, T. and Terrill, E. J.: Skill assessment of resolving ocean surface current structure using compact-antenna-style HF radar and the MUSIC direction-finding algorithm, J. Atmos. Ocean. Tech., 24, 1277–1300, 2007.

De Paolo, T., Terril, E., and Kirincich, A.: Improving SeaSonde radial velocity accuracy and variance using radial metrics, IEEE Oceans 2015, Genova, Italy, 1–9, 2015.

Emery, B., Washburn, M. L., and Harlan, J. A.: Evaluating radial current measurements from CODAR high frequency radars with moored current meters, J. Atmos. Ocean. Tech., 21, 1259–1271, 2004.

Emery, B. M. and Washburn, L.: Evaluation of SeaSonde Hardware Diagnostic Parameters as Performance Metrics, NOAA IOOS final report, October 2007 CA, USA, 2007.

Emery, W. J. and Thomson, R. E.: Data Analysis Methods in Physical Oceanography, Elsevier Science, Amsterdam, the Netherlands, 2001.

Espino, M., Sanchez-Arcilla, A., and Garcia, M. A.: Wind induced mesoscale circulation off the Ebro Delta, NW Mediterranean: a numerical study, J. Marine Syst., 16, 235–251, 1998.

Font, J.: A comparison of seasonal winds with currents on the continental slope of the Catalan sea (Northwestern Mediterranean), J. Geophys. Res., 95, 1537–1545, 1990.

Font, J., Salat, J., and Tintore, J.: Permanent features of the circulation in the Catalan Sea, Pelagic Mediterranean Oceanography, Oceanol. Acta, 9, 51–57, 1988a.

Font, J., Salat, J., and Wang, D. P.: Lagrangian and Eulerian observation of inertial oscillations in the shelf break offshore the Ebro River Delta (Catalan Sea, NW Mediterranean), Rapp. Comm. Int. Mer Médit, 31, p. 2, 1988b.

Font, J., Garcia-Ladona, E. and Gorriz, E. G.: The seasonality of mesoscale motion in the Northern Current of the Western Mediterranean: several years of evidence, Oceanol. Acta, 18, 207–219, 1995.

Garcia, M. A. and Ballester, A.: Notas acerca de la meteorología y la circulación local en la región del Delta del Ebro, Invest. Pesquera (now Sci. Mar.) 48, 469–493, 1984.

Gomez, R., Helzel, T., Petersen, L., Kniephoff, K., Merz, C. R., Liu, Y., and Weisberg, R. H.: Real-time quality control of current velocity data on individual grid cells in WERA HF radar, Oceans 2014, Taipei, Taiwan, 7–10 April 2014, 1–7, 2014.

Gomez, R., Helzel, T., Merz, C. R., Liu, Y., Weisberg, R. H., and Thomas, N.: Improvements in ocean surface radar applications through real-time data quality-control, Conference: Current, Waves and Turbulence Measurement (CWTM), IEEE/OES, 2–6 March 2015, Florida, USA, 2015.

Gonella, J.: A rotary-component method for analyzing meteorological and oceanographic vector time series, Deep-Sea Res. Pt II, 19: 833–846, 1972.

Graber, H. C., Haus, B. K., Shay, L. K., and Chapman, R. D.: HF radar comparisons with moored estimates of current speed and direction: Expected differences and implications, J. Geophys. Res., 102, 749–766, 1997.

Jimenez, J. A., Guillen, J., Sanchez-Arcilla, A., Gracia, V., and Palanques, A.: Influence of benthic boundary layer dynamics on wind-induced currents in the Ebro Delta inner shelf, J. Geophys. Res., 107, 1–10, 2002.

Kaplan, D. M. and Lekien, F.: Spatial interpolation and filtering of surface current data based on open-boundary modal analysis, J. Geophys. Res.-Oceans (1978–2012), 112, 1–20, 2007.

Kaplan, D. M., Largier, J., and Botsford, L. W.: HF radar observations of surface circulation off Bodega Bay (northern California, USA), J. Geophys. Res., 110, 1–25, 2005.

Kaihatu, J. M., Handler, R. A., Marmorino, G. O., and Shay, L. K.: Empirical orthogonal function analysis of ocean surface currents using complex and real-vector methods, J. Atmos. Ocean. Tech., 15, 927–941, 1998.

Kirincich, A. R., de Paolo, T., and Terrill, E.: Improving HF Radar Estimates of Surface Currents Using Signal Quality Metrics, with Application to the MVCO High-Resolution Radar System, J. Atmos. Ocean. Tech., 29, 1377–1390, 2012.

Kohut, J. T. and Glenn, S. M.: Improving HF radar surface current measurements with measured antenna beam patterns, J. Atmos. Ocean. Tech., 20, 1303–1316, 2003.

Kovačević, V., Gačić, M., Mancero Mosquera, I., Mazzoldi, A., and Marinetti, S.: HF radar observations in the northern Adriatic: surface current field in front of the Venetian Lagoon, J. Marine Syst., 51, 95–122, 2004.

Kundu, P.: Ekman veering observed near the ocean bottom, J. Phys. Oceanogr., 6, 238–242, 1976.

Kundu, P. K. and Allen, J. S.: Some three-dimensional characteristics of low-frequency current fluctuations near the Oregon coast, J. Phys. Oceanogr. 6, 181–199, 1976.

Levanon, N.: Lowest GDOP in 2-D scenarios, IEEE Proceedings, Radar, Sonar Navigation, 147, 149–155, 2000.

Lipa, B., Nyden, B., Ullman, D. S., and Terrill, E.: SeaSonde radial velocities: derivation and internal consistency, IEEE J. Oceanic Eng., 31, 850–861, 2006.

Liu, Y., Weisberg, R. H., and Merz, C. R.: Assessment of CODAR SeaSonde and WERA HF Radars in Mapping Surface Currents on the West Florida Shelf, J. Atmos. Ocean. Tech., 31, 1363–1382, 2014.

Lorente, P., Piedracoba, S., Soto-Navarro, J., and Alvarez-Fanjul, E.: Accuracy assessment of high frequency radar current measurements in the Strait of Gibraltar, Journal of Operational Oceanography, 7, 59–73, 2014.

Lorente, P., Piedracoba, S., Soto-Navarro, J., Ruiz, M. I., Alvarez-Fanjul, E., and Montero, P.: Towards the implementation of a fully operational HF coastal radar network operated by Puertos del Estado, IEEE Oceans 2015, Genova, Italy, 1–6, 2015a.

Lorente, P., Piedracoba, S., and Alvarez-Fanjul, E.: Validation of high-frequency radar ocean surface current observations in the NW of the Iberian Peninsula, Cont. Shelf Res. 92, 1–15, 2015b.

Lorente, P., Piedracoba, S., Soto-Navarro, J., and Alvarez-Fanjul, E.: A combined QC methodology in Ebro Delta HF radar system: real time web monitoring of diagnostic parameters and offline validation of current data, European Geosciences Union General Assembly (EGU), 12–17 April 2015, Vienna, Austria, 2015c.

Marmain, J., Molcard, A., Forget, P., and Barth, A.: Assimilation of HF radar surface currents to optimize forcing in the North Western Mediterranean sea, Nonlinear Proc. Geophy., 21, 659–675, 2014.

Münchow, A. and Chant, R. J.: Kinematics of inner shelf motions during the summer stratified season off New Jersey, J. Phys, Oceanogr., 30, 247–268, 2000.

North, G. R., Bell, T. L., Cahalan R. F., and Moeng, F. J.: Sampling errors in the estimation of empirical orthogonal functions, Mon. Weather Rev., 110, 699–706, 1982.

Ohlmann, C., White, P., Washburn, L., Terril, E., Emery, B., and Otero, M.: Interpretation of coastal HF radar-derived currents with high-resolution drifter data, J. Atmos. Ocean. Tech., 24: 666–680, 2007.

Paduan, J. D., Kim, K. C., Cook, M. S., and Chavez, F. P.: Calibration and validation of direction-finding High-Frequency radar ocean surface current observations, IEEE J. Oceanic Eng., 31, 862–875, 2006.

Robinson, A. M., Wyatt, L. R., and Howarth, M. J.: A two year comparison between HF radar and ADCP current measurements in Liverpool Bay, Journal of Operational Oceanography, 4, 33–45, 2011.

Roarty, H., Smith, M., Kerfoot, J., Kohut, J., and Glenn, S.: Automated Quality Control of High Frequency Radar Data, IEEE Oceans 2012, 1–7, 2012.

Rypina, I. I., Kirincich, A. R., Limeburner, R., and Udovydchenkov, I. A.: Eulerian and Lagrangian Correspondence of

High-Frequency Radar and Surface Drifter Data: Effects of Radar Resolution and Flow Components, J. Atmos. Ocean. Tech., 31, 945–966, 2014.

Salat, J., Garcia, M. A., Cruzado, A., Palanques, A., Arín, L., Gomis, D., Guillen, J., de León, A., Puigdefàbregas, J., Sospedra, J., and Velásquez, Z. R.: Seasonal changes of water mass structure and shelf-slope exchanges at the Ebro Shelf (NW Mediterranean), Cont. Shelf Res., 22, 327–348, 2002.

Schmidt, R.: Multiple emitter location and signal parameter estimation, IEEE T. Antenn. Propag., 34, 276–280, 1986.

Solabarrieta, L., Rubio, A., Castanedo, S., Medina, R., Charria, G., and Hernández, C.: Surface water circulation patterns in the southeastern Bay of Biscay: New evidences from HF radar data, Cont. Shelf Res., 74, 60–76, 2014.

Sotillo, M. G., Cailleau, S., Lorente, P., Levier, B., Aznar, R., Reffray, G., Amo-Baladrón, A., and Alvarez-Fanjul, E.: The MyOcean IBI Ocean Forecast and Reanalysis Systems: Operational products and roadmap to the future Copernicus Service, Journal of Operational Oceanography, 1–18, 2015.

Stanev, E. V., Ziemer, F., Schultz-Stellenfleth, J., Seemann, J., Staneva, J., and Gurgel, K. W.: Blending Surface Currents from HF Radar Observations and Numerical Modelling: Tidal Hindcasts and Forecasts, J. Atmos. Ocean. Tech., 32, 256–281, 2015.

Taylor, K. E.: Summarizing multiple aspects of model performance in a single diagram, J. Geophys. Res., 106, 7183–7192, 2001.

Trujillo, D. A., Kelly, F. J., Perez, J. C., Riddles, H. R., and Bonner, J. S.: Accuracy of Surface Current Velocity Measurements Obtained from HF Radar in Corpus Christi Bay, Texas, IEEE/IGARSS Int. Geosci. Remote. Se., 2, 1179–1182, 2004.

Wyatt, L.: Improving the quality control and accuracy of HF radar currents, IEEE Oceans 2015, Genova, Italy, 1–9, 2015.

Yoshikawa, Y., Masuda, A., Marubayashi, K., Ishibashi, M., and Okuno, A.: On the accuracy of HF radar measurement in the Tsushima strait, J. Geophys. Res., 111, C04009, doi:10.1029/2005JC003232, 2006.